A study of lithium ion batteries cycle aging by thermodynamics techniques

Kenza Maher [b], Rachid Yazami [a,b,∗]

[a] Nanyang Technological University, School of Materials Science and Engineering and Energy Research Institute at Nanyang (ERIAN), Research Techno Plaza, X-Frontier Blk, 50 Nanyang Drive, Singapore 637553, Singapore
[b] TUM CREATE, 1 Create Way, #10-02 Create Tower, Singapore 138602, Singapore

A B S T R A C T

Lithium ion batteries (LiB) are cycled under a galvanostatic regime (∼C/2-rate) between 2.75 V and 4.2 V for up to 1000 cycles. After each completed 100 cycles, the discharge capacity, capacity loss, average discharge potential were determined under the same C/2 rate. Then cells undergo an additional charge and discharge cycle at C/6 rate followed by a thermodynamics measurements test. This enables open-circuit potential (OCP), entropy (ΔS) and enthalpy (ΔH) data to be assessed.

It is found that with increasing cycle number, the entropy and enthalpy profiles show more significant changes than those observed in the discharge and the OCP curves especially at particular SOC and OCP values. These differences are attributed to the higher sensitivity of entropy and enthalpy state functions to changes in the crystal structure of the graphite anode and the lithiated cobalt oxide (LCO) induced by cycle aging compared to the free energy ΔG (OCP) alone. The thermodynamics data are supported by post-mortem X-ray diffractometry (XRD) and Raman scattering (RS) analyses on the electrode materials. The results show important LCO crystal structure degradation, whereas, surprisingly, the graphite anode remains almost unaffected by heavy cycling, if not improved.

© 2013 Elsevier B.V. All rights reserved.

1. Introduction

It is common knowledge that rechargeable batteries in general and LiB in particular will experience a natural decrease in energy storage performance upon extended cycling [1–8]. The main parameters controlling battery performance decaying with cycle number, N are: 1) depth of discharge (DOD) [1,9,10], 2) depth of charge (DOC) [10,11], 3) rates of charge and discharge [12–14], 4) temperature [15–19], 5) over-charge [20–22], and 6) over-discharge [19]. Performance decay with N includes decreased discharge capacity and average discharge potential [1,10,12–14], decreased power output [5,17,23] and increased internal resistances [12,24–26]. Performance decay originates from degradation of electrode and electrolyte materials upon aging and occasionally from losses in electrical contacts

between active materials in the anode, cathode and current collector [27].

In this study LiB coin cells were cycled under constant charge and discharge rate of ∼C/2 between 2.75 V and 4.2 V at ambient temperature in 100 cycle batches for up to 1000 cycles. After each 100 cycles, the cells underwent an additional charge and discharge cycle under C/6-rate enabling discharge capacity ($q_d(N)$) and average discharge potential ($<e_d(N)>$) to be assessed. Then a thermodynamics measurements test on the cells was run following which entropy and enthalpy data were collected and plotted vs. SOC and OCP.

We found well defined SOC and OCP areas where entropy and enthalpy data show significant changes compared with barely detectable changes in the corresponding discharge and OCP profiles. Differences in data resolution between entropy and enthalpy on one hand and OCP on the other hand are attributed to amplified changes in thermodynamics characteristics of anode and cathode with cycle aging at particular SOC and OCP values where phase transitions and phase conversion takes place.

Post-mortem XRD and RS analyses performed on anode and cathode of a fresh cell and of a 1000 times cycled cell provide direct evidence for LCO crystal structure degradation and graphite structure resilience if not, surprisingly, enhancement.

∗ Corresponding author. Nanyang Technological University, School of Materials Science and Engineering and Energy Research Institute at Nanyang (ERIAN), Research Techno Plaza, X-Frontier Blk, 50 Nanyang Drive, Singapore 637553, Singapore.

E-mail address: rachid@ntu.edu.sg (R. Yazami).

2. Experimental

2.1. Cycling condition and capacity loss determination

LiB coin-cells (2032, rated ∼44 mAh) are used in this study. Cells were cycled between 2.75 V and 4.2 V under 20 mA constant current (∼C/2-rate) at the ambient temperatures using an Arbin Instruments Battery Cycler. After each completed 100 cycles, the cells discharge capacity, capacity loss, average discharge potential and energy under the same C/2-rate were determined.

2.2. Thermodynamics measurements and state of charge determination

After each finished 100 cycles cells are transferred to the Electrochemical Thermodynamics Measurement System instrument (ETMS, Battery Analyzer BA-1000®, KVI PTE LTD, Singapore) to run following sub-steps:

a Conditioning cycle: Cells are charged to 4.2 V under C/6 rate then a constant 4.2 V was applied until the current dropped below 0.05 mA (∼C/900). Cells were then discharged to 2.75 V under C/6-rate and a constant 2.75 V voltage was held until current drops again below 0.05 mA. In this cycle the ETMS determines the cells' charge and discharge capacity. The later is used to determine the SOC during the next step.
b Electrochemical Thermodynamics Measurements (ETM) test in which the cells are charged by 5% increments up to 4.2 V at C/6 rate where SOC = 100%. At each SOC the cells temperature T is decreased from the ambient temperature (∼25 °C) to 10 °C by 5 °C steps and the cells' OCP is monitored. After the last temperature step at 10 °C is completed the temperature is left to rise to 25 °C then an additional 5% increment is applied to the SOC. This enables entropy and enthalpy to be determined according to Eqs. (1) and (2), respectively.

$$\Delta S(x) = F\left(\frac{\partial E_0(x,T)}{\partial T}\right)_{x,p} \tag{1}$$

$$\Delta H(x) = -F\left(E_0(x,T) + T\left(\frac{\partial E_0(x,T)}{\partial T}\right)_{x,p}\right) \tag{2}$$

where $E_0(x,T)$ is the OCP at temperature T, x = SOC, F = Faraday constant, p = pressure

The same cells were then cycled again for an additional 100 cycles until reaching 1000 cycles.

At the end of 1000 cycles, one cell out of four used in this study was discharged to 2.75 V and opened in a dry box filled with argon. The anode and cathode were then washed with DMC dried in vacuum, and mechanically separated from their respective copper and aluminum substrates. Electrode powders were analyzed by XRD (Bruker D8 Advance diffractometer) using CuK$_\alpha$ radiation in the angular range of 15°–90° (2θ) for cathode and 20°–90° (2θ) for anode with 0.02° 2θ-step, and by Raman scattering RS spectrometry, using Renishaw inVia Raman microscope in the backscattering geometry at room temperature. Excitation was carried out with the 514 nm radiation of an argon ion laser of 20 mW power.

3. Results and discussion

3.1. Discharge results

Fig. 1a and b shows the discharge profiles vs. discharge capacity q_d (mAh) and vs. normalized capacity (or state of discharge SOD),

respectively. Fig. 2a and b shows both discharge capacity and average discharge voltage $<e_d>$ decreased with N, as one expects. Reported in Table 1 are the discharge characteristics data including $q_d(N)$, $<e_d(N)>$, discharge energy $E_d(N) = q_d(N) \times <q_d(N)>$ and capacity $q_{CL}(N)$ loss given by:

$$q_{CL}(N) = \frac{q_d(1) - q_d(N)}{q_d(1)} \times 100 \tag{3}$$

($q_d(1)$ = discharge capacity after 1 cycle). The $E_d(N)$ trace displayed in Fig. 2c varies almost linearly ($R = 99.3\%$) with N according to:

$$E_d(N)(mWh) = 133.6 - 0.0527 \times N \tag{4}$$

$E_d(N)$ dropped by 22% and 39% after 500 and 1000 cycles, respectively corresponding to an average decrease rate of 0.094% per cycle.

The cells' OCP profiles vs. q_d and SOC are traced in Fig. 3a and b, respectively. Contrarily to the OCP vs. q_d profiles, which show significant variation with N, the OCP vs. SOC curves in Fig. 3b lay on top of each, except at 0% and 5% SOC values. The OCP vs. SOC results should relate to the fact that at each SOC (and at constant temperature and pressure), the cathode and the anode equilibrium potentials; $E_0^+(SOC,N)$ and $E_0^-(SOC,N)$ depend only on the lithium stoichiometry in the active fraction of cathode and anode. After each cycle the fraction of active anode and active cathode decreases. Because SOC normalizes the active part of anode and cathode to 100%, the OCP given in Eq. (5) will vary a little with N, which explains the superposition of the OCP vs. SOC curves.
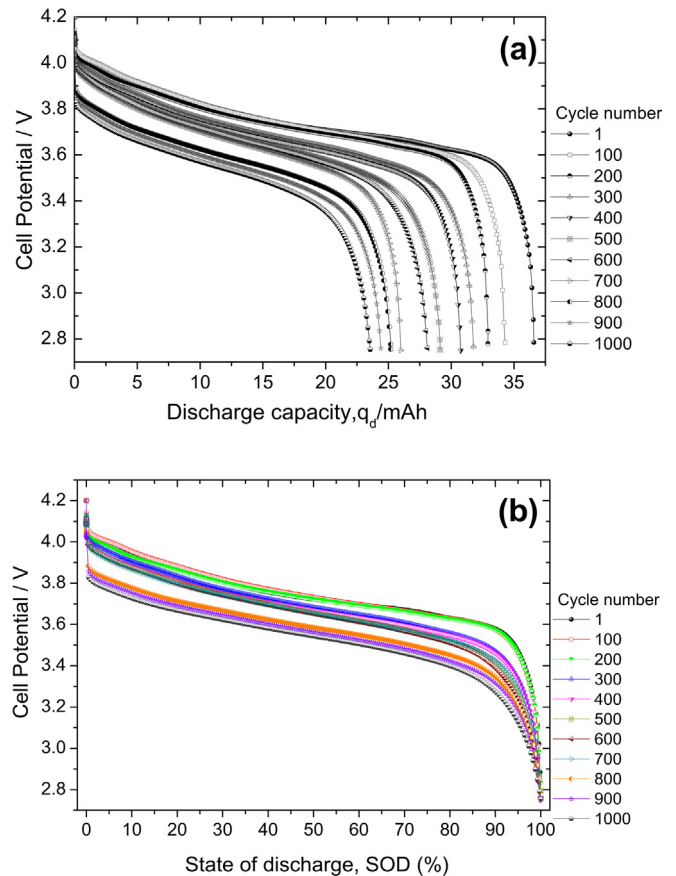

Fig. 1. Discharge profiles (C/2-rate) of LiB cells after cycling vs. discharge capacity (a) and vs. state of discharge (SOD).
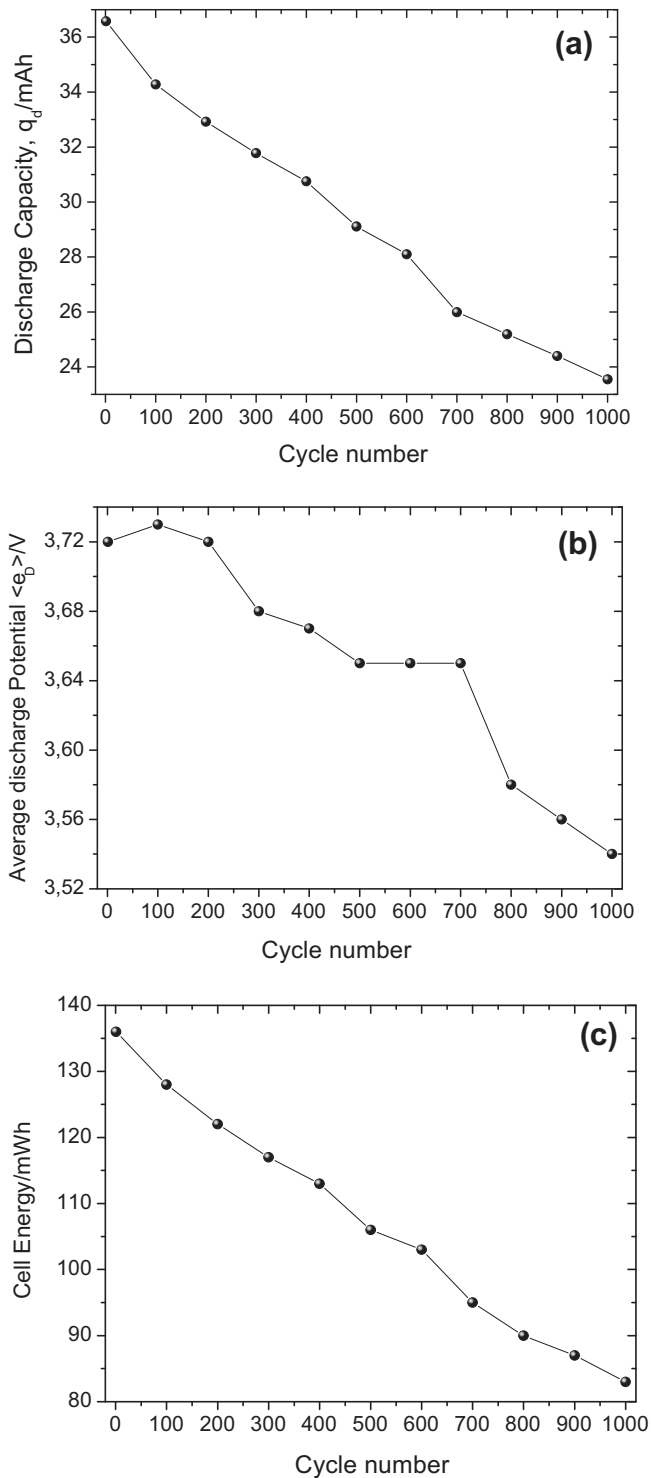
Table 1
Discharge capacity, average discharge potential, capacity loss and discharge energy of LIB cells data with cycle number.

Cycle number	q_d (mAh)	q_{CL}(%)	$<e_d>$ (V)	E_d (mWh)
1	36.58	–	3.72	136
100	34.28	6.3	3.73	128
200	32.92	10	3.72	122
300	31.78	13.1	3.68	117
400	30.75	15.9	3.67	113
500	29.11	20.4	3.65	106
600	28.10	23.2	3.65	103
700	25.99	28.9	3.65	95
800	25.19	31.1	3.58	90
900	24.40	33.3	3.56	87
1000	23.55	35.62	3.54	83

vacancies in the cathode will affect the OCP value. Moreover, we also reported an important change in entropy and enthalpy in the graphite anode around 5% SOC relating to the phase transition from graphite to dilute stage-1 lithium–graphite intercalation compound [29]. Such a steep change in thermodynamics properties of the graphite anode should account for the OCP data dispersion at 5% SOC.
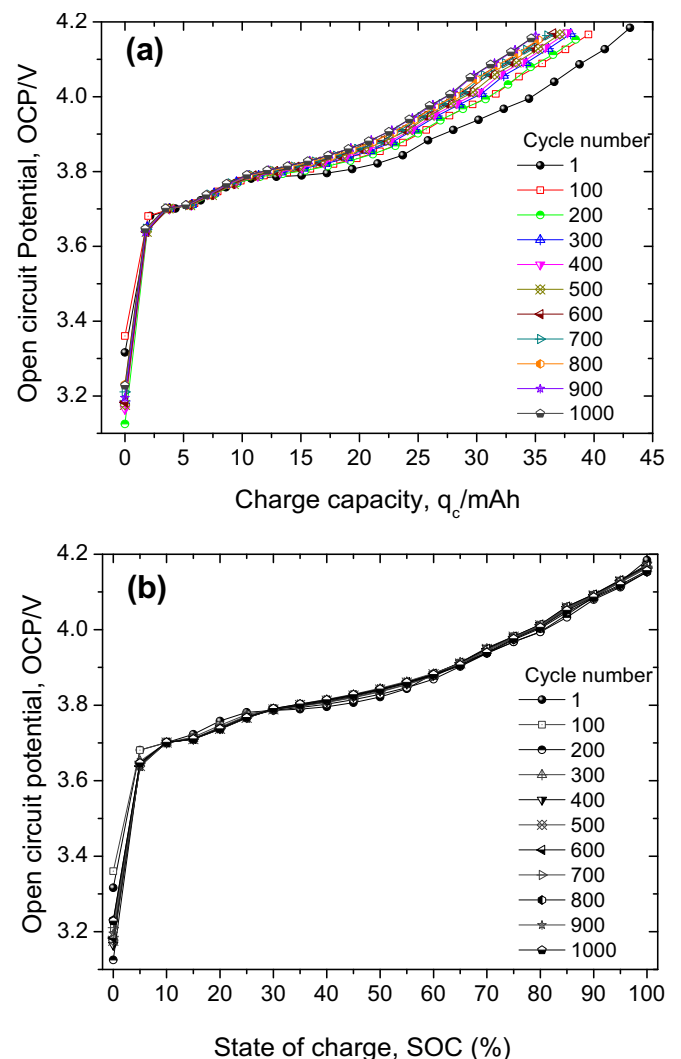

Fig. 2. Cells capacity profile (a), average discharge potential (b) and energy (c) vs. cycle number.

$$OCP = E_0^+(SOC, N) - E_0^-(SOC, N) \qquad (5)$$

The OCP data dispersion at 0% SOC (discharged state at 2.75 V) in Fig. 3a should be attributed to residual lithium present in the graphite anode and/or of lithium vacancies in the LCO cathode as shown in our recent study performed on identical LiB cells aged at high temperatures [28]. Residual lithium in the anode and lithium

Fig. 3. Open circuit potential profile of cycled LIB cells vs. capacity (a) and vs. SOD (b).

3.2. Entropy and enthalpy data

Fig. 4a and b shows the entropy profiles of cycled cells vs. SOC and OCP, respectively and Fig. 5a and b shows the corresponding enthalpy profiles. Insets in Figs. 4a and b, 5a and b highlight SOC and OCP areas where changes in entropy and enthalpy data are relatively important. Specifically, the area around 70%, 85% and 90% SOC in Fig. 4a and the area around 3.95 V, 4.05−4.06 V and 4.075−4.08 V in Fig. 4b are those within which entropy and enthalpy profiles show the most significant changes.

As discussed in our recent thermodynamics studies on identical LiB cells during thermal [28] and overcharge [30] aging, the above mentioned particular SOC and OCP areas are associated with crystal structure changes in LCO cathode including, 1) reversible phase transition from hexagonal to monoclinic symmetry, and 2) irreversible conversion from hexagonal to cubic (spinel) symmetry.

Although observable in the enthalpy profiles in Fig. 5a and b, the changes in the particular SOC and OCP areas are less pronounced than in the associated entropy curves of Fig. 4a and b, respectively. One possible explanation of difference between entropy and enthalpy may originate from that entropy is more sensitive to structural disorder and phase transformation than the enthalpy is. Configurational (mixing) entropy in a solid solution system is given by:

$$S(x) = -k[x\ln x + (1-x)\ln(1-x)] \qquad (6)$$

where x = fraction of Li$^+$ occupied sites in graphite and in LCO and k = Boltzmann's constant.

Derivation of Eq. (6) yields:

$$\Delta S(x) = \left(\frac{\partial S(x)}{\partial x}\right)_{T,p} = -k\ln\frac{x}{1-x} \qquad (7)$$

Accordingly, $\Delta S(x)$ should increase steadily at phase transition around $x = 1$.

By contrast, enthalpy relates to heat generated by M−O (M = Co, Li) bonds breaking and reconstruction and/or by MO$_6$ octahedra and MO$_4$ tetrahedra distortion at phase transition, both being finite. Therefore, the entropy contribution to the free energy should be higher than that of enthalpy.

Another interesting feature in Figs. 4a and 5a is the small change, if any in the entropy and enthalpy values, respectively at 5% SOC. As pointed out above, at 5% SOC the graphite anode undergoes a phase transition from graphite to dilute stage-1 lithium graphite intercalation compound [29]. The energetics of such a transition is affected by changes in the crystal structure of the graphite anode. Since entropy and enthalpy values at 5% SOC vary little with N, the anode crystal structure should remain unaffected with cycle aging. This later result strongly contrasts with our previous thermodynamics studies during overcharge and thermal aging where we reported important changes in the entropy and enthalpy data at 5% SOC. Accordingly, the performances decay in LiB upon cycling at the ambient temperatures is controlled by the LCO cathode structure degradation rather than that of the anode. Our statement is further supported by post mortem analyses on anode and cathode by XRD and RS discussed in the next section.
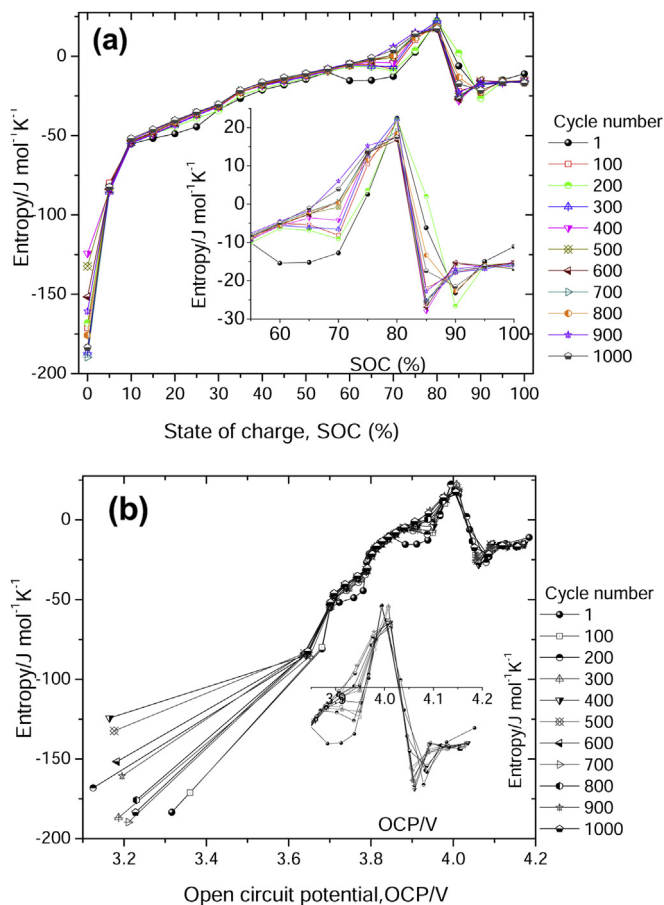

Fig. 4. Entropy profiles of cycled LIB cells during charge vs. state of charge (a) and vs. open-circuit potential (b).
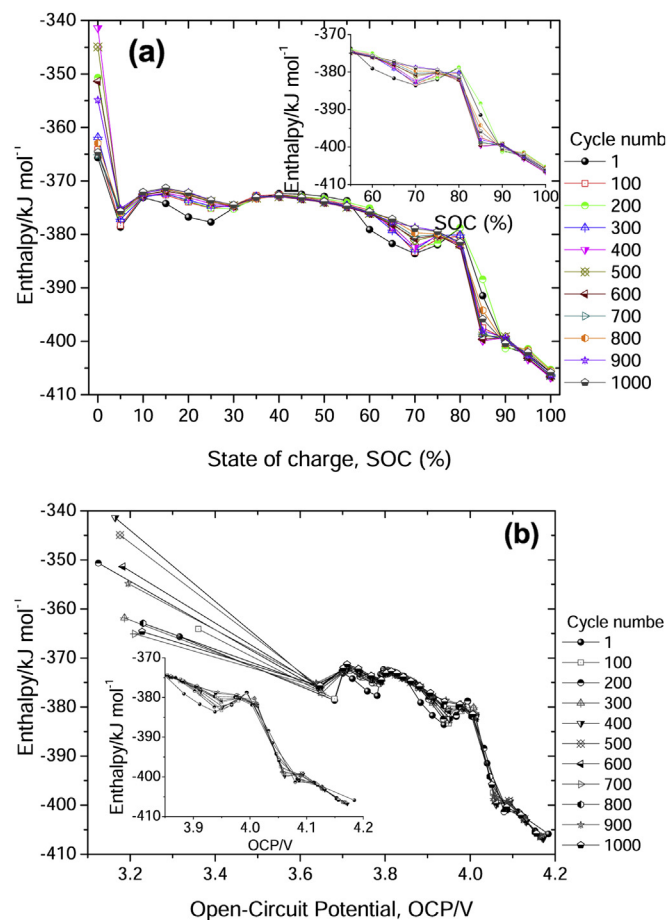

Fig. 5. Enthalpy profiles of cycled LIB cells during charge vs. state of charge (a) and vs. open-circuit potential (b).
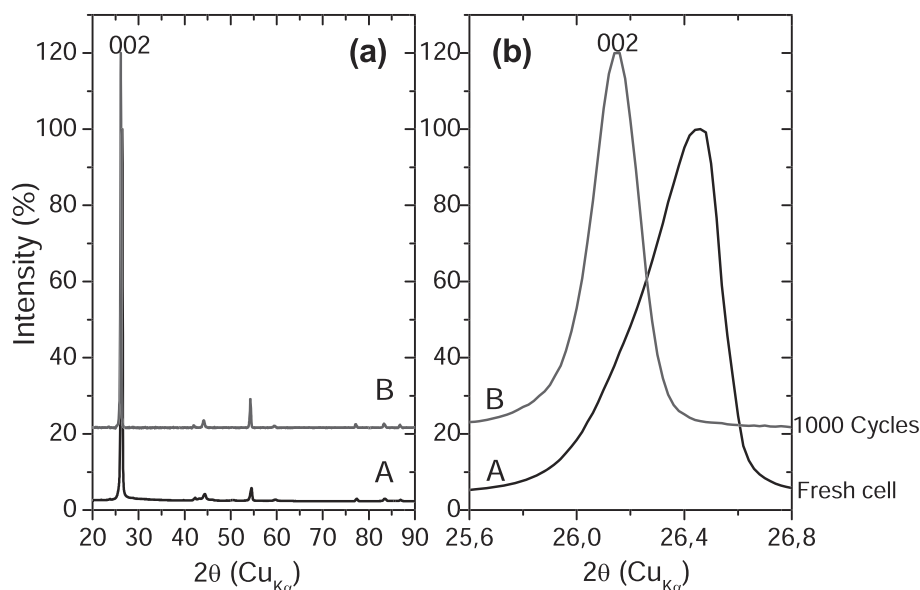
Fig. 6. X-ray diffractograms of graphite anode material taken from a fresh LIB cell (A) and from a 1000 cycle cell (B); full spectrum (a) and in the 002 peak area (b).

3.3. XRD and Raman characterization

3.3.1. Graphite anode

The XRD and the RS analyses data performed on the graphite anode and the LCO cathode taken from a fresh ($N = 1$) cell and from a cell after 1000 cycles will be compared here. Fig. 6a shows extended X-ray diffractograms of the graphite anode before (A) and after (B) 1000 cycles. Fig. 6b highlights the 002 peak area ($25.6° \leq 2\theta \leq 26.8°$). The graphite 002 peak of the cycled sample shifted to lower angles and became narrower. A shift to lower angles of the 002 peak suggests the presence of residual lithium in the graphite structure ($Li_\varepsilon C_6$, $\varepsilon \sim 0$) due to incompleteness of Li ion de-intercalation [31,32]. We found similar results in overcharge and thermally aged identical LiB cells [28,30]. Residual lithium in the discharged anode should be due to kinetic reasons such as growth of a more and more resistive solid electrolyte interphase (SEI) on the surface of the graphite anode particles upon cycling [33–35]. Such a resistive SEI hinders lithium from complete transfer from the electrode to the electrolyte at the end of discharge. The SEI formation should also account for the cells' irreversible capacity loss since lithium is consumed during the SEI growth and for lower average discharge potentials as displayed in Table 1.

The narrowing of the 002 peak after 1000 cycles is a less expected result. It suggests an enhancement of the graphite crystal structure during the cells' extended cycling. At the ambient temperatures and under mild charge and discharge rates such as C/2, within the potential window of 2.75 V–4.2 V, the graphite crystal structure is not expected to degrade much owing to a highly protective SEI. By contrast, during high temperatures and overcharge aging, the SEI dissolves in the electrolyte and/or degrades leading to enhanced permeability to the organic solvent molecules present in the electrolyte [28,30]. Solvent molecules tend co-intercalate into the graphite causing crystal structure degradation and huge c-parameter expansion (exfoliation) [36].

Moreover, XRD data show the graphite anode material used in the cells has an interlayer spacing of 3.37 Å (002 peak position of $2\theta = 26.45°$ in Fig. 6b (A)). 3.37 Å is sizeably higher than 3.35 Å characteristic of carbons with 100% graphitization degree [37]. Accordingly, the graphite anode has imperfect crystallinity, which goes with an initial broad 002 peak.

Structural disorder in the graphite anode is also supported by the RS data displayed in Fig. 7. The two typical active modes of disordered graphite; the D-mode at 1350 cm^{-1} and the G-mode at 1580 cm^{-1} are present in both fresh and cycled anode samples. The D-mode is attributed to in-plane domain size effects [38–40]. As shown in Fig. 7 the relative intensity of the D-mode remains almost unchanged before and after cycling. Such a feature does not conflict with possible enhanced stacking order of the graphene layers upon repetitive lithium intercalation and de-intercalation. In such a process graphene layers glide on each other to form AA stacking in LiC_6 from initial ABAB and ABCABC stacking in hexagonal and rhombohedral graphite, respectively. Repetitive layers gliding upon cycling may end up healing the stacking defects in the starting graphite anode material, therefore, improving crystallinity as reported in Refs. [41,42].

3.3.2. LCO cathode

Fig. 8a shows XRD patterns of the LCO cathode before (A) and after 1000 cycles (B) and Fig. 8b and c focus on areas around the 003
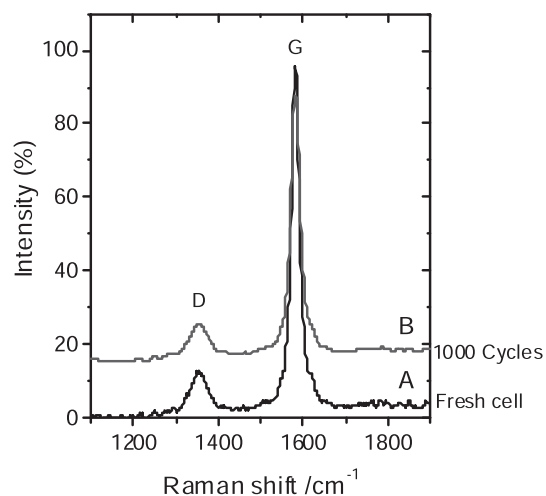

Fig. 7. Raman spectra of graphite anode material taken from a fresh LIB cell and from a 1000 cycle cell.

and the 104 peaks, respectively. Upon cycling both the 003 and 104 peaks shifted to lower angles and broadened. Moreover, the 003 peak split into two peaks.

The crystal structure effect of long cycle aging is stronger in LCO than in graphite. A shift in the 003 and 104 peaks position to lower angles should come from lithium deficiencies in discharged LCO. Ideally, the LCO composition should vary between Li_1CoO_2 and $Li_{\sim 0.5}CoO_2$ in discharge and charge states, respectively. As lithium de-intercalates from Li_1CoO_2 to form $Li_{1-x}CoO_2$ during charge, the c-parameter of the hexagonal LCO phase expands while the a-parameter varies a little, causing the 003 and 104 peaks to shift towards lower angles [43—47]. In the charged state at 4.2 V, the LCO composition is about $Li_{0.5}CoO_2$. During the next discharge lithium re-intercalates into LCO. However, because active lithium is irreversibly lost during the SEI formation and in residue in the anode, LCO becomes lithium deficient at the end of discharge, causing the shift in the 003 and the 104 peaks.

On the other hand the splitting in two of the 003 peak shown in Fig. 8b should be due to the irreversible conversion of hexagonal LCO to cubic spinel. Such a conversion is thermodynamically favored in the charged (de-lithiated) state [48,49]. As a matter of fact, the RS data displayed in Figs. 9A and 8B on LCO sample before and after aging give evidence of the spinel formation. Fig. 9A shows the two typical active modes of the hexagonal LCO O$_3$ phase ($R\overline{3}m$ symmetry) E_g^h and A_{1g}^h modes at 595 cm^{-1} and 486.7 cm^{-1}, respectively [48,50,51]. Upon cycling a new peak appears around
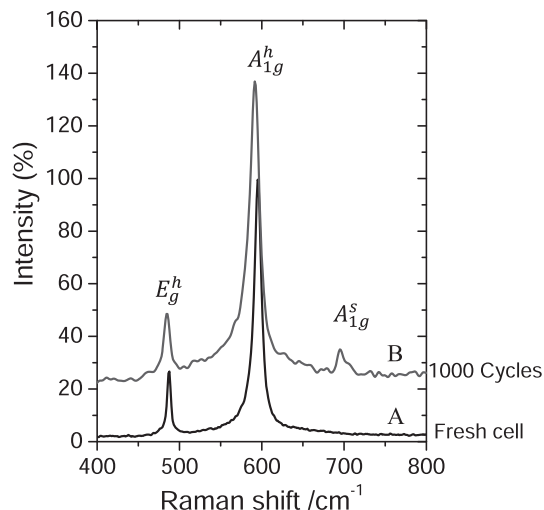

Fig. 9. Raman spectra of LCO cathode material taken from a fresh LIB cell and from a 1000 cycle cell.

700 cm^{-1} as shown in Fig. 9B. The later is characteristic of A_{1g}^s mode in spinel LCO (Fd3m symmetry) [28,30,52]. Moreover, E_g^h both and A_{1g}^h modes shifted to lower frequencies and broadened in the cycled sample. This denotes a weakening of the Li—O and M—O lattice bond energy as hexagonal LCO gradually converts into spinel via a cation mixing mechanism [47].

4. Conclusion

The effect of long cycling of graphite anode and LCO cathode based LiB cells on the discharge performances and thermodynamics properties has been investigated. We found the energy output decreased quasi-linearly with the cycle number at a rate of $\sim 0.094\%$ per cycle. The OCP vs. SOC profiles are not affected by the cycle number, except at 0% and 5% SOC values. Large differences appeared in the entropy and enthalpy profiles vs. both SOC and OCP upon cycling compared to OCP vs. SOC data. The most pronounced changes in entropy and enthalpy data took place around 75%, 85% and 90% SOC and around 3.95 V, 4.05 V and 4.075 V OCP, respectively. These particular SOC and OCP areas are associated with crystal structure transformations taking place in the LCO cathode. At $\sim 5\%$ SOC where the effect of the anode on thermodynamic properties is expected to be more important, there is no significant change in entropy and enthalpy data, suggesting that the anode remained basically unaffected by cycling.

XRD and Raman scattering performed on anode and cathode before and after 1000 cycles provided evidence for resilience of the anode towards extended cycling at ambient temperature. This strongly contrasts with the LCO cathode structure, which was found to irreversibly degrade, therefore controlling the decay in the LiB cells electrochemical performances.

Fig. 8. X-ray diffractograms of LCO cathode material taken from a fresh LIB cell and from a 1000 cycle cell; full spectrum (a), 003 peak are (b) and 104 peak area (c).

References

[1] D. Linden, T.B. Reddy (Eds.), Handbook of Batteries, third ed., McGrow-Hill Handbooks, 2002, pp. 22.3—22.24.
[2] P. Ramadass, B. Haran, R. White, B.N. Popov, J. Power Sources 112 (2002) 606.
[3] K. Takei, K. Kumai, Y. Kobayashi, H. Miyashiro, N. Terada, T. Iwahori, T. Tanaka, J. Power Sources 97—98 (2001) 697.
[4] K. Sawai, R. Yamato, T. Ohzuku, Electrochim. Acta 51 (2006) 1651.
[5] M. Broussely, in: W.A.V. Schalkwijk, B. Scrosati (Eds.), Advances in Lithium-ion Batteries, Kluwer Academic/Plenum Publishers, New York, 2002, p. 393.
[6] S. Santhanagopalan, Q. Zhang, K. Kumaresan, R.E. White, J. Electrochem. Soc. 155 (2008) A345.
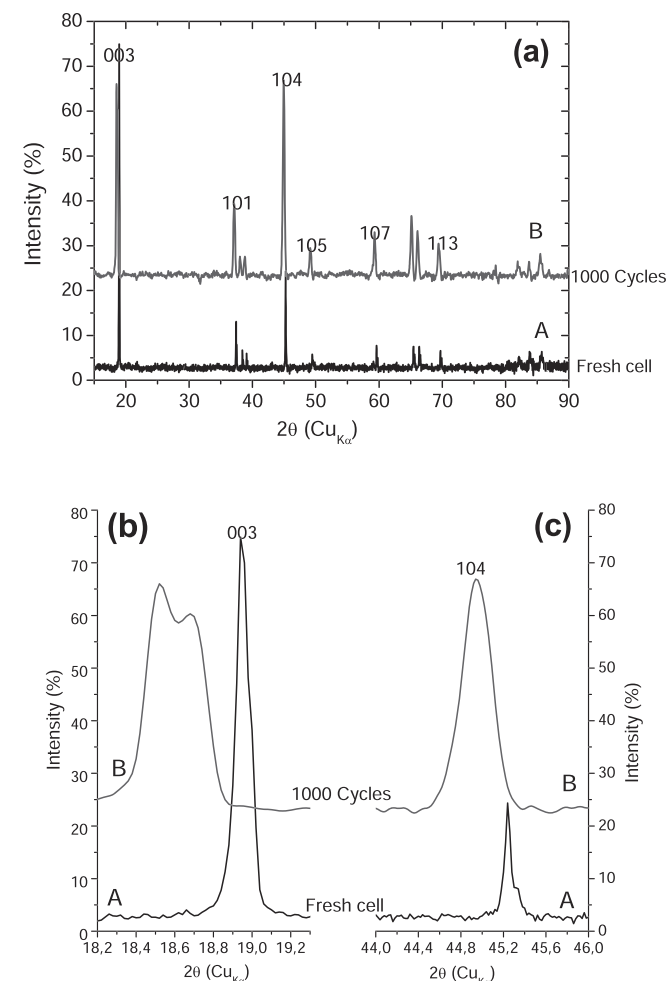[7] P. Ramadass, B. Haran, R. White, B.N. Popov, J. Power Sources 111 (2002) 210.

[8] G.C. Bruce, L. Marcoux, IEEE Aerosp. Electr. Syst. Mag. 16 (2001) 24–28.
[9] X.M. Wang, Y. Sone, H. Naito, C. Yamada, G. Segami, K. Kibe, J. Power Sources 160 (2006) 602–608.
[10] G. Ning, B.N. Popov, J. Electrochem. Soc. 151 (2004) A1584.
[11] M. Majima, H. Yoshida, E. Yagasaki, T. Tada, Y. Oka, K. Miyazaki, in: C.F. Holmes, A.R. Landgrebe (Eds.), Proc. Symp. Batt. Port. Appl. Elec. Vehicles, Electrochem. Soc. Ser, vol. 97, 1997, p. 362.
[12] J. Li, E. Murphy, J. Winnick, P.A. Kohl, J. Power Sources 102 (2001) 294.
[13] Y.H. Ye, Y.X. Shi, N.S. Cai, J. Lee, X.M. He, J. Power Sources 199 (2012) 227.
[14] K.C. Lim, A.M. Lackner, P.O. Braatz, W.H. Smith, J.D. Margerum, H.S. Lim, in: Proceedings of the Symposium Batteries for Portable Applications and Electric Vehicles, vol. 97–181, The Electrochemical Society, Paris, France, 31 August–5 September, 1997, p. 470.
[15] R.B. Wright, C.G. Motloch, J.R. Belt, J.P. Christophersen, C.D. Ho, R.A. Richardson, I. Bloom, S.A. Jones, V.S. Battaglia, G.L. Henriksen, T. Unkelhaeuser, D. Ingersoll, H.L. Case, S.A. Rogers, R.A. Sutula, J. Power Sources 110 (2002) 445–470.
[16] J. Shim, R. Kostecki, T. Richardson, X. Song, K.A. Striebel, J. Power Sources 112 (2002) 222–230.
[17] J.R. Belt, C.D. Ho, T.J. Miller, M.A. Habib, T.Q. Duong, J. Power Sources 142 (2005) 354–360.
[18] B.A. Johnson, R.E. White, J. Power Sources 70 (1998) 48–54.
[19] J. Vetter, P. Novak, M.R. Wagner, C. Veit, K.C. Moller, J.O. Besenhard, M. Winter, M. Wohlfahrt-Mehrens, C. Vogler, A. Hammouche, J. Power Sources 147 (2005) 269.
[20] S.S. Choi, Hong S. Lim, J. Power Sources 111 (2002) 130.
[21] R.A. Leising, M.J. Palazzo, E.S. Takeuchi, K.J. Takeuchi, J. Power Sources 97 (2001) 681.
[22] W. Lu, C.M. Lopez, N. Liu, J.T. Vaughey, A. Jansen, D.W. Dees, J. Electrochem. Soc. 159 (2012) A566.
[23] T. Horiba, T. Maeshima, F. Matsumura, M. Koseki, J. Arai, Y. Muranaka, J. Power Sources 146 (2005) 107–110.
[24] R. Kostecki, F. McLarnon, in: I.V. Barsukov, C.S. Johnson, J.E. Doninger, V.Z. Barsukov (Eds.), NATO Science Series, Series II: Mathematics, Physics and Chemistry, vol. 229, 2006, pp. 445–452.
[25] Y.C. Zhang, C.Y. Wang, J. Electrochem. Soc. 156 (2009) A527–A535.
[26] D. Aurbach, B. Markovsky, A. Rodkin, M. Cojocaru, E. Levi, H.J. Kim, Electrochim. Acta 47 (2002) 1899–1911.
[27] J. Zhu, K.Y. Zeng, L. Lu, Electrochim. Acta 68 (2012) 52–59.
[28] K. Maher, R. Yazami, Electrochim. Acta 101 (2013) 71.
[29] D. Billaud, F. Henry, P. Willmann, Mol. Cryst. Liq. Cryst. 244 (1994) 159.
[30] K. Maher, R. Yazami, J. Power Sources 247 (2013) 527–533.
[31] Y.F. Reynier, R. Yazami, B. Fultz, J. Electrochem. Soc. 151 (2004) A422–A426.
[32] R. Kostecki, F. McLarnon, J. Power Sources 119 (2003) 550.
[33] E. Markevich, G. Salitra, M.D. Levi, D. Aurbach, J. Power Sources 146 (2005) 146.
[34] J. Li, J. Zhang, X. Zhang, C. Yang, N. Xu, B. Xia, Electrochim. Acta 55 (2010) 927.
[35] M.E. Spahr, H. Wilhelm, T. Palladino, N. Dupont-Pavlovsky, D. Goers, F. Joho, P. Novak, J. Power Sources 119 (2003) 543–549.
[36] Y. Reynier, R. Yazami, B. Fultz, I. Barsukov, J. Power Sources 165 (2007) 552.
[37] F. Tuinstra, J.L. Koenig, J. Chem. Phys. 53 (1970) 1126.
[38] K. Nakamura, M. Fujitsuka, M. Kitajima, Phys. Rev. B 41 (1990) 12260.
[39] M. Inaba, H. Yoshida, Z. Ogumi, T. Abe, Y. Mizutani, M. Asano, J. Electrochem. Soc. 142 (1995) 20.
[40] M.A. Pimenta, G. Dresselhaus, M.S. Dresselhaus, L.G. Cancado, A. Jorio, R. Saito, Phys. Chem. Chem. Phys. 9 (2007) 1276.
[41] L.J. Hardwick, M. Marcinek, L. Beer, J.B. Kerr, R. Kostecki, J. Electrochem. Soc. 155 (2008) A442.
[42] C.N. Barnakov, A.,P. Kozlov, S.K. Seit-Ablaeva, in: B.Q. Li, Z.Y. Liu (Eds.), Prospects for Coal Science in the 21st Century, 1999, pp. 133–136.
[43] A.,R. Ubbelohde, Mat. Sci. Eng. 31 (1977) 341–350.
[44] T. Ohzuku, A. Ueda, J. Electrochem. Soc. 141 (1994) 2972.
[45] G.G. Amatucci, J.M. Tarascon, L.C. Klein, J. Electrochem. Soc. 143 (1996) 1114.
[46] Z. Chen, Z. Lu, J.R. Dahn, J. Electrochem. Soc. 149 (2002) A1604.
[47] Y. Ozawa, R. Yazami, B. Fultz, J. Power Sources 119 (2003) 918.
[48] H. Gabrisch, R. Yazami, B. Fultz, J. Electrochem. Soc. 151 (2004) A891.
[49] G. Ceder, A. Van der Ven, Electrochim. Acta 45 (1999) 131.
[50] L. Mendoza, R. Baddour-Hadjean, M. Cassir, J.P. Pereira-Ramos, Appl. Surf. Sci. 225 (2004) 356.
[51] M. Inaba, Y. Todzuka, H. Yoshida, Y. Grincourt, A. Tasaka, Y. Tomida, Z. Ogumi, Chem. Lett. 10 (1995) 889.
[52] C. Julien, Solid State Ionics 136–137 (2000) 887.